PAPER • OPEN ACCESS

First-passage times in complex energy landscapes: a case study with nonmuscle myosin II assembly

To cite this article: Rick Bebon and Ulrich S Schwarz 2022 *New J. Phys.* **24** 063034

New Journal of Physics
The open access journal at the forefront of physics

Deutsche Physikalische Gesellschaft DPG
IOP Institute of Physics

Published in partnership with: Deutsche Physikalische Gesellschaft and the Institute of Physics

OPEN ACCESS

RECEIVED
6 April 2022

REVISED
4 June 2022

ACCEPTED FOR PUBLICATION
15 June 2022

PUBLISHED
30 June 2022

PAPER

First-passage times in complex energy landscapes: a case study with nonmuscle myosin II assembly

Rick Bebon[1] and **Ulrich S Schwarz**[*]

Institute for Theoretical Physics and BioQuant, Heidelberg University, Heidelberg, Germany
[*] Author to whom any correspondence should be addressed
[1] Current address: Mathematical BioPhysics Group, Max Planck Institute for Multidisciplinary Sciences, Göttingen, Germany

E-mail: schwarz@thphys.uni-heidelberg.de

Keywords: stochastic dynamics, coarse-graining, master equation, molecular motors, self-assembly

Abstract

Complex energy landscapes often arise in biological systems, e.g. for protein folding, biochemical reactions, or intracellular transport processes. Their physical effects are frequently reflected in the first-passage times (FPTs) arising from these energy landscapes. However, their calculation is notoriously challenging and it is often difficult to identify the most relevant features of a given energy landscape. Here we show how this can be achieved by coarse-graining the Fokker–Planck equation to a master equation and decomposing its FPTs in an iterative process. We apply this method to the electrostatic interaction between two rods of nonmuscle myosin II (NM2), which is the main molecular motor for force generation in nonmuscle cells. Energy landscapes are computed directly from the amino acid sequences of the three different isoforms. Our approach allows us to identify the most relevant energy barriers for their self-assembly into NM2 minifilaments and how they change under force. In particular, we find that antiparallel configurations are more stable than parallel ones, but also show more changes under mechanical loading. Our work demonstrates the rich dynamics that can be expected for NM2-assemblies under mechanical load and in general shows how one can identify the most relevant energy barriers in complex energy landscapes.

1. Introduction

The concept of an energy landscape provides a powerful theory approach that has led to a unified description of many complex natural phenomena in numerous different physical systems [1]. If depicted graphically, such systems resemble mountainous landscapes with many hills and valleys. While notable examples from chemistry and condensed matter physics include chemical kinetics [2, 3] or glass-forming systems [4–6], in a biophysical context, energy landscapes are central for explaining a wide range of biomolecular processes [7]. For example, they help to understand the folding and conformational dynamics of proteins [1, 8], including single-molecule experiments [9, 10], where details of the underlying multidimensional energy landscape can be inferred from transition paths of low-dimensional projections [10]. They also provide perspectives on the structure and dynamics of the entire genome [11] and help us understanding the microscopic origins of selective transport processes through membrane channels [12–15]. Moreover, the general notion of diffusion on energy landscapes has been proven to be successful for e.g. modeling molecular motors [16, 17], where motor-specific landscapes have been obtained from molecular structures [18–20] or using single-molecule trajectories [21–23].

Very often, the main aspect of interest for diffusive motion in a multi-well energy landscape is the first-passage time (FPT) [24–26], i.e. the time when a stochastic process first passes a prescribed threshold value. FPTs tend to have a broad probability distribution, yet the average value mean first-passage time (MFPT), often captures main physical aspects of complex systems. Moreover, FPT-distributions and more so MFPTs do not require a complete solution of the stochastic equations and therefore tend to be more accessible. Many biophysical systems have been successfully analyzed along these lines, including the kinetics

of chemical reactions [27–31], enzyme catalysis [32–34], molecular search processes [35–39], signaling in biological cells [40–44], cell adhesion [45–49], modeling of molecular motors [50, 51], self-assembly processes [52], protein folding kinetics [53, 54], and single-molecule pulling experiments by atomic force spectroscopy [55–61]. More broadly, first-passage theory is central to the description of diverse problems ranging from foraging behavior of animals or bacteria [62–66], population dynamics [38, 67], and the spread of infectious diseases [68–70], to transport in disordered media [71], or the dynamics of financial markets and stock options [72].

While substantial advances have been achieved in the theory of first-passage processes on flat energy landscapes for finite domains [31, 35, 73], much less is known about first-passage properties for more general rough energy landscapes [74]. Usually such results are restricted to simple model landscapes and do not address the complex energy landscapes typically encountered in biological systems. For instance, it was found that the introduction of finite potential barriers may lead to a reduction in the MFPT [75] which subsequently allows for the optimization of escape rates [76], and that intermediate barriers may accelerate the rate of barrier crossing events [77]. Moreover, it has been shown that FPT distributions provide a link between the dynamical properties and the topology of complex networks [78]. For one-dimensional discrete-state dynamics these theoretical results made it possible to quantitatively infer key features of energy landscapes from measurements of the FPT distribution. A characteristic power-law regime for the short-time statistics of the FPT was demonstrated to reflect e.g. the number and depth of intermediate potential minima in experiments on different length scales [79]. Furthermore, a recently discovered duality between FPT and relaxation processes for reversible Markovian dynamics provided further insight into FPT phenomena in rugged energy landscapes [80, 81]. Yet a more general understanding of the first-passage properties for general rough landscapes is still missing.

In this paper, we use a specific biophysical example to demonstrate how in general the MFPT can be calculated for highly complex and rugged one-dimensional energy landscapes by coarse-graining the dynamics following the continuous overdamped Fokker–Planck equation into a discrete master equation. As our case study, we use self-assembly of the molecular motor nonmuscle myosin II (NM2). Myosins constitute a diverse superfamily of motor proteins that generate mechanical work by converting chemical energy produced during ATP-hydrolysis into conformational changes that eventually propel actin filaments forward [82, 83]. The myosin II subfamily is a class of non-processive molecular motor proteins that have to work in sufficiently large ensembles to generate force. This is achieved by self-assembly into bipolar filaments, which are present not only in muscle cells, but also in nonmuscle cells, where NM2 forms so-called minifilaments that are composed of up to 30 NM2 molecules (each with two motor heads) with a typical size of 300 nm [84–86]. NM2 is the main force generator in nonmuscle cells and crucial for many essential cellular functions, including adhesion, migration, division, and mechanosensing. While NM2 traditionally has been investigated mainly using electron microscopy [87, 88], super-resolution microscopy has made it possible to break the 200 nm resolution limit of traditional light microscopy, allowing the investigation of NM2 minifilaments dynamics in live cells [89–93]. These live-cell imaging studies demonstrated that besides *de novo* filament formation, the proliferation of NM2 minifilaments is additionally driven by novel partitioning mechanisms like filament splitting and reveal unexpected processes such as expansion, concatenation, long-range attraction and stacking. Adding to the notion that NM2 minifilaments are far more dynamic than formerly appreciated, it was observed that individual NM2 monomers are characterized by high exchange rates [92] and that the three human NM2-variants (A, B, C) co-assemble into mixed filaments with distinct characteristics [94–96]. Thus the question arises how the energy landscapes of these assemblies look like and how the system explores its different configurations.

NM2-molecules assemble by forming parallel and antiparallel staggers of their rod-like regions. This interaction is mainly of electrostatic origin and determined by the amino acid sequence of the respective rods [97–101]. Earlier modeling approaches were able to predict the experimentally observed staggers as local minima of the electrostatic interaction energy landscape, but also led to very noisy data [99–101]. A detailed three-dimensional molecular model of the NM2 rod structure provided better data quality of the energy landscape, but again identified the known staggers only as local minima [98]. Recently, the identification of staggers were improved considerably by introducing the concept of MFPTs into the modeling of NM2-staggering [97]. Modeling in addition the splaying of NM2-molecules in a rolling and zipping motion as part of the energy landscape, the experimentally observed staggers emerged as maxima in the MFPT (e.g. contact time) as function of the initial alignment. Thus by replacing energies by MFPTs, the physical stability of these systems became more apparent.

Although resulting in many interesting predictions on the stability of competing staggers, the earlier work did not identify the decisive features of the energy landscape that lead to these staggers. It also did not consider the effect of mechanical force, that is essential for the functioning of NM2-minifilaments and that might stabilize new configurations or completely destabilize the assembly. Here we will use systematic and

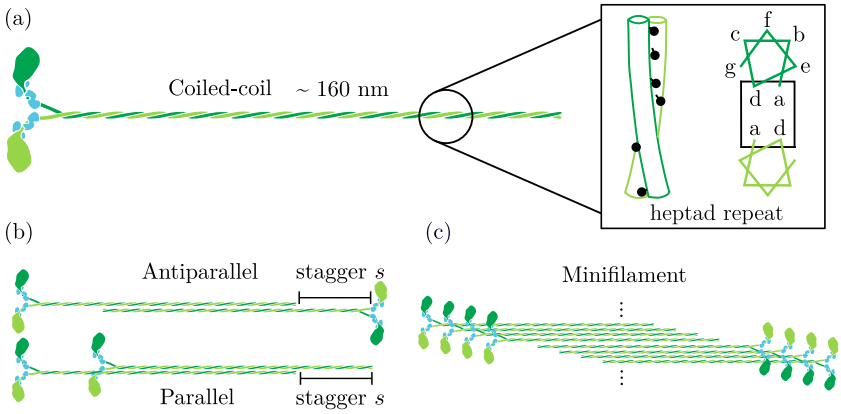

Figure 1. NM2 structure and assembly. (a) A NM2-molecule is mainly comprised of two identical heavy chains (light and dark green) that begin with a motor head domain at the N-terminal domain and end with the nonhelical tail at the C-terminal. In addition, four light chains attach at the neck (blue). The rod part of the molecule consists of a 160 nm long coiled-coil region in which the heavy chains wind around each other with a pitch of 3.5 residues per turn. The coiled-coil is stabilized by the heptad repeat (*a* to *g*) of the amino acid sequence of each heavy chain (inset). Residues at position *a* and *d* form a hydrophobic interface and the remaining residues are exposed to the surrounding. (b) The electrostatic interactions of the exposed residues of the heptad repeats lead to either parallel or antiparallel staggers of the NM2-dimers. (c) Self-assembly of up to 30 NM2-molecules forms the bipolar minifilaments with a typical size of 300 nm.

rigorous coarse-graining of the complex energy landscapes to address these important questions for the assembly of NM2-molecules. In order to be able to conduct a comprehensive analysis of a one-dimensional model, here we consider only straight myosin II rods and disregard the effects of bending. Our work does not only give new and interesting results for NM2-assembly, but also demonstrates how a successful coarse-graining procedure can be implemented for complex one-dimensional energy landscapes in general.

2. Derivation of the energy landscapes

2.1. Structural model and charge distribution of NM2-rod domains

In order to give an instructive example of a complex one-dimensional energy landscape with many potential barriers of different height, we first introduce the case of the self-assembly of NM2-molecules into minifilaments. As schematically depicted in figure 1(a), one NM2 monomer consists mainly of two identical myosin II heavy chains (shown in light and dark green) that dimerize to form its rigid helical backbone. Hereby, each heavy chain begins with a globular motor head domain at the N-terminal containing bindings sites for actin filaments as well as for ATP-molecules. Following the head region comes a neck region in which two regulatory light chains and two essential light chains bind (shown in blue). Then comes the roughly 160 nm long and relatively rigid coiled-coil rod and finally the non-helical tailpiece that disrupts the coiled-coil motif. Although the whole complex is in fact a hexamer, here we call it a NM2-molecule for simplicity. In the coiled-coil rod domain the two heavy chains wind around each other with an axial spacing of 0.1456 nm between adjacent residues and a pitch of 3.5 residues per turn due to interactions between periodically placed hydrophobic residues [102, 103]. For this purpose, each NM2 heavy chain features an amino acid sequence with a heptad repeat labeled from *a* to *g* as schematically depicted in the inset of figure 1(a). Here, residues at positions *a* and *d* form the hydrophobic interface between two adjacent side chains, whereas the remaining residues are hydrophilic and exposed to the solvent. The assembly of the NM2-molecules into dimers is mediated by the electrostatic interactions of the exposed residues, whose charge pattern leads to either parallel or antiparallel staggers, as shown in figure 1(b). The predominance of electrostatic driving forces during the assembly process was demonstrated by *in vitro* experiments where an increase in salt concentration was found to inhibit filament formation due to electrostatic screening effects [104]. The final minifilament contains up to 30 NM2-molecules, is bipolar and around 300 nm large, compare figure 1(c).

The derivation of the electrostatic interaction energy between two NM2-molecules relies on the procedures recently introduced in reference [97]. First the amino acid sequence of the coiled-coil rod domain of individual NM2-molecules, as provided by the *NCBI protein database* [105], is translated into a linear chain of point-charges. We have analyzed the amino acid sequences of the three human NM2-isoforms (denoted as NM2A, NM2B and NM2C) via the sequence-based coiled-coil prediction software *Paircoil*2 [106]. By employing pairwise residue probabilities [107], *Paircoil*2 is able to identify the location of coiled-coil motifs in protein amino acid sequence data. Performing this statistical analysis yields

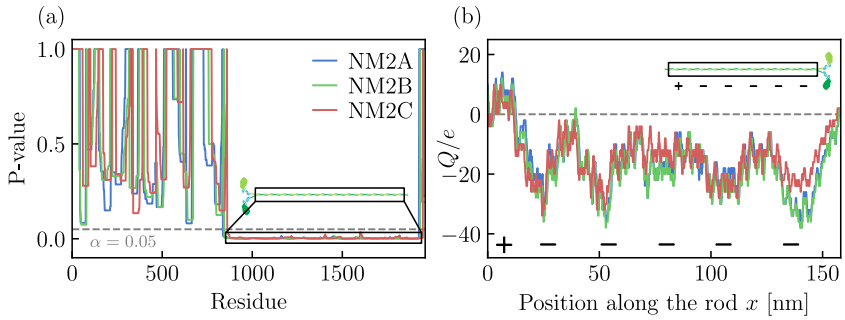

Figure 2. Analysis of NM2 amino acid sequences. (a) Prediction of the coiled-coil region for different NM2-isoforms obtained with the software package *Paircoil2* [106]. The dashed grey line denotes the significance level of $\alpha = 0.05$ indicating that residues from roughly 850 to 1920 are part of the coiled-coil motif. Remaining residues on the left and right correspond to the head and to the non-helical tailpiece, respectively. (b) Charge distribution along the NM2-rod treated as a chain of linear charges. Summation with a sliding window of 98 residues highlights the expected positively charged C-terminal tip which is followed by five negatively charged regions along the whole rod domain.

a *p*-value for each individual residue of the sequence data, which in turn allows us to test the null hypothesis whether the respective residue is *not* located within a coiled-coil domain. As depicted in figure 2(a), this hypothesis is *rejected* for a domain ranging from roughly the 850th up to the 1920th amino acid residue for all NM2-variants, indicating that these residues are indeed part of the coiled-coil motif of the NM2 heavy chain. The first large non coiled-coil region indicates the motor and neck region, whereas the small region at the end of the amino sequence represents the non-helical tailpiece (compare figure 1(a)).

After identifying the NM2 coiled-coil motif (∼1100 out of total ∼2000 amino acids) and the positions of individual residues along the rod, we are now able to associate all required amino acids of the coiled-coil with their corresponding charges. Amino acids at residue position *a* and *d* are hereby assigned zero net charge as they face inwards and form the *hydrophobic* coiled-coil backbone (compare inset in figure 1(a)). The remaining residue positions are either assigned a charge of '$+2e$' for positively charged amino acids (i.e. arginine and lysine) or '$-2e$' for negatively charged amino acids (i.e. glutamic acid and aspartic acid). Moreover point-like charges are arranged with an axial spacing of $\Delta x = 0.1456$ nm between adjacent neighbors [97, 102, 103] which subsequently yields the correct dimensions for the NM2-molecule length of approximately 160 nm. The corresponding distribution of charges along the NM2 coiled-coil rod domain is depicted in figure 2(b) for all three different NM2-variants. For clarity, we hereby smooth the distribution of charges via a sliding window of 98 residues [97, 99]—the preferred axial shift between interacting molecules due to the 196 residue repeat—which allows us to identify the positive C-terminal tip assembly critical domain (ACD), and the five regions with negative charge spaced along the rod domain. We note that the quantitative difference between the different NM2-variants is comparatively small.

2.2. Electrostatic interaction

The $+ - - - - -$ charge pattern revealed in figure 2(b) is the physical basis of the self-assembly of minifilaments and has been identified before by similar procedures [97–99]. In line with these previous modeling approaches, our calculations of energy landscapes are restricted to the electrostatic interactions of two aligned NM2-molecules which are based on the charge distribution calculated in section 2.1. For simplicity we do not account for bending of NM2 rods that has been used before by including bending energies to complement the electrostatic interactions [97] as it would require additional numerical procedures and effectively renders the energy landscapes two-dimensional. We also neglect potential contributions of the entropy of segment bending to the free energy. Because the persistence length of the myosin II rods is 130 nm [108, 109] and dangling parts to the polymers are usually in the same order of magnitude or less, such contributions are expected to contribute only little in our context. To calculate the electrostatic interaction energy between two rods, we note that under physiological salt concentrations we are in the weak coupling regime for a rod with 0.085 e per residue, a distance 0.1456 nm between residues and a radius 1 nm [97]. Thus the appropriate treatment of electrostatics is Poisson–Boltzmann theory [110, 111]. Our considered system is additionally characterized by small ionic strengths, allowing us to linearize the Poisson–Boltzmann equation, yielding the Debye–Hückel equation

$$\nabla^2\psi(\mathbf{r}) = \kappa^2\psi(\mathbf{r}). \tag{1}$$

Here ψ denotes the electrostatic potential and κ is the inverse Debye–Hückel screening length that sets the typical length scale of the electrostatic screening.

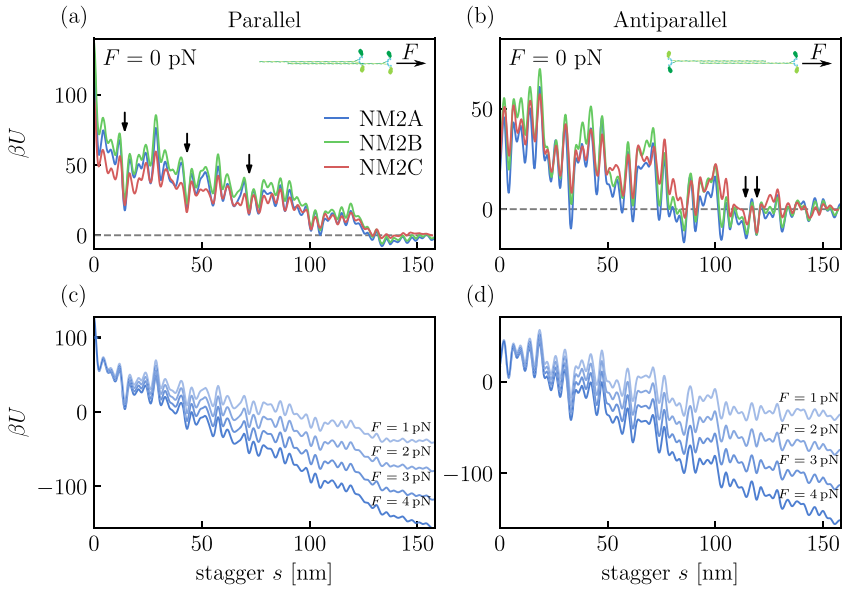

Figure 3. Energy landscapes of the electrostatic interaction for two NM2-molecules for variable pulling force F. Landscapes for all three NM2 variants without external pulling in either (a) parallel or (b) antiparallel configurations and as a function of their respective stagger s in units of the thermal energy $k_BT = 1/\beta$. NM2-monomers are aligned with a lateral distance of $y = 2$ nm. Experimentally known staggers (black arrows) are local minima in the energy landscapes. Application of an variable external pulling force $F > 0$ pN tilts the (c) parallel and (d) antiparallel energy landscape as explicitly shown for the NM2A-dimer.

To now compute the electrostatic interaction energy of two aligned NM2 rods, each modeled as a linear chain of charges, we always have to consider two different cases. As schematically illustrated in figure 1(b), NM2-molecules assemble in either *parallel* or *antiparallel* fashion, and they may align with a different stagger s. For the geometry of a single point-particle with charge q, it is possible to analytically solve equation (1), resulting in a Yukawa-type potential [110] of the form

$$\psi(r) = \frac{q}{4\pi\epsilon\epsilon_0}\frac{\exp(-\kappa r)}{r}. \tag{2}$$

Exploiting the linearity of the Debye–Hückel equation (1) furthermore allows us to directly compute the total electrostatic interaction energy $U(s)$ of two aligned NM2-rods as a function of their stagger s as

$$U(s) = \sum_{i=1}^{N}\sum_{j=1}^{M}\frac{q_i q_j}{4\pi\epsilon\epsilon_0}\frac{\exp(-\kappa r_{ij})}{r_{ij}}, \tag{3}$$

where we define $r_{ij} \equiv \sqrt{y^2 + [(i-j)\Delta x - s]^2}$ as the distance between residues. Point charges are denoted with q whereas N and M denote the total number of residues of the respective rods with i and j as their corresponding index. The distance along the NM2 rod, i.e. the main axis, is given by x, while y denotes the lateral spacing between two aligned NM2-molecules. In the case of an antiparallel NM2-dimer configuration we invert one of the two charge sequences.

The resulting electrostatic interaction energy landscapes for NM2-dimers are shown in figures 3(a) and (b) as a function of the stagger s and in units of the thermal energy $k_BT = 1/\beta$ for parallel and antiparallel configurations, respectively. By calculating the interaction energy according to equation (3) we assume a lateral spacing of $y = 2$ nm [87, 97]. Moreover, we do not take negative staggers into account as their positive ACDs would not be in contact with the negative charged region, i.e. their interaction would become highly unfavorable. The experimentally known staggers ($s = 14.3$ nm, $s = 43.2$ nm and $s = 72.0$ nm for parallel alignment and $s = 113$ nm to $s = 118$ nm for antiparallel alignment) are marked in figures 3(a) and (b) by black arrows and emerge as local minima generated by the electrostatic interaction between the positive ACD and regions with increased net negativity along the NM2-rod. However, as noted earlier, these minima are not very clear, which motivates our approach to use these energy landscapes to investigate the corresponding FPT-problems.

To investigate situations in which the NM2-dimer is being pulled apart, e.g. due to contractile forces in the actomyosin network, we study the impact of an external pulling force F on the energy landscape. Force-mediated rearrangements may be of particular importance at the beginning stages of minifilament assembly and during the dynamical partitioning of minifilaments [91, 112], when filaments physically split

into a pair of two 'daughter' filaments. To account for the mechanical load we apply an additional constant external pulling force $F > 0$ pN along the stagger main-axis coordinate in positive s-direction. As seen in figures 3(c) and (d) for parallel and antiparallel alignment, respectively, this driving leads to a tilted NM2-dimer energy landscape

$$\beta U^{(F)}(s) = \beta U_0(s) - \beta F s, \tag{4}$$

where $U_0 \equiv U^{(0\,\mathrm{pN})}(s)$ denotes the electrostatic potential energy as given by equation (3) of the original 'untilted' NM2-dimer.

3. Mean-first passage time until detachment

In order to better identify relevant staggers during NM2-assembly, we next compute the average time that passes until a NM2-dimer detaches from a certain initial value for the stagger. In the biologically relevant overdamped limit, the probability density $p(s, t)$ to find the system at some time t with a stagger s evolves according to the Fokker–Planck equation

$$\partial_t p(s, t) = \mathcal{L} p(s, t), \tag{5}$$

where $\mathcal{L} = -\partial_s A(s, t) + \partial_s^2 B(s, t)$ denotes the Fokker–Planck operator. The drift term is determined by the external potential in the form of $A = -\mu \partial_s U(s)$ where μ is the mobility coefficient (i.e. inverse friction coefficient). Moreover, the stochastic contribution of the Brownian motion is described by the diffusion constant via the Einstein relation $B = D = \mu/\beta$, where β denotes the inverse thermal energy.

We define the one-dimensional domain of interest $[a, b]$ of the detachment process as follows. The absorbing boundary b is set to the maximal possible stagger (or minimal overlap) between two aligned NM2 rods, i.e., where the stagger is equal to the complete rod length such that $b = 1085\Delta x \approx 157.98$ nm for rods with 1085 amino acid residues. Reaching the absorbing target therefore corresponds to the detachment of the NM2-dimer and marks the end of the process. The reflecting boundary a is placed at the minimal stagger (or maximal overlap) with $a = 0$ nm, which corresponds to the complete alignment with the maximal overlap of the complete NM2 rod length. Since the systems behavior is described by absorbing and reflecting boundaries, our FPT-problem is characterized by mixed boundaries with $a < b$.

The backward Fokker–Planck framework introduces an efficient way of calculating the nth moment $\mathcal{T}_n$ of the first-passage time density by employing the recurrence relation [113–115]

$$\mathcal{L}^\dagger \mathcal{T}_n = -n\mathcal{T}_{n-1} \tag{6}$$

with $\mathcal{T}_0 = 1$ and where $\mathcal{L}^\dagger = A(s_0, t)\partial_{s_0} + B(s_0, t)\partial_{s_0}^2$ denotes the backward Fokker–Planck operator. For a diffusion process subject to the NM2 energy landscape equation (3), the MFPT ($n = 1$) consequently can be obtained by solving the ordinary differential equation

$$\mathcal{L}^\dagger \mathcal{T}_1(s_0) = -1. \tag{7}$$

In our case of mixed boundary conditions with $a < b$, the solution of equation (7), i.e. the MFPT $\mathcal{T}_1$, is given by the well known formula [113–115]

$$\mathcal{T}_1(s_0) = \int_{s_0}^{b} \frac{\mathrm{d}y}{\Psi(y)} \int_a^y \mathrm{d}z \, \frac{\Psi(z)}{B(z)}, \tag{8}$$

where we define

$$\Psi(z) \equiv \exp\left(\int^z \mathrm{d}x \, \frac{A(x)}{B(x)} \right) = \exp(-\beta U(z)) \tag{9}$$

by inserting the drift velocity A and diffusion coefficient B as they enter the Fokker–Planck equation (5). The final analytical expression for the MFTP time now reads

$$\mathcal{T}_1(s_0) = \frac{1}{D} \int_{s_0}^{b} \mathrm{d}y \, \mathrm{e}^{\beta U(y)} \int_a^y \mathrm{d}z \, \mathrm{e}^{-\beta U(z)}. \tag{10}$$

To calculate the MFTP for landscapes of different NM2-dimer variants we numerically solve equation (10) after inserting the corresponding electrostatic interaction energy $U(s)$ from equation (3) for different NM2-variants and configuration. Here the two integrals are solved numerically using the trapezoid rule function `integrate.trapezoid` as implemented in the python library `SciPy` [116]. Throughout the remainder of this paper, we make the diffusion coefficient dimensionless, $D = 1$, since we are interested in the relative differences of the average detachment time between all NM2-variants and configurations and

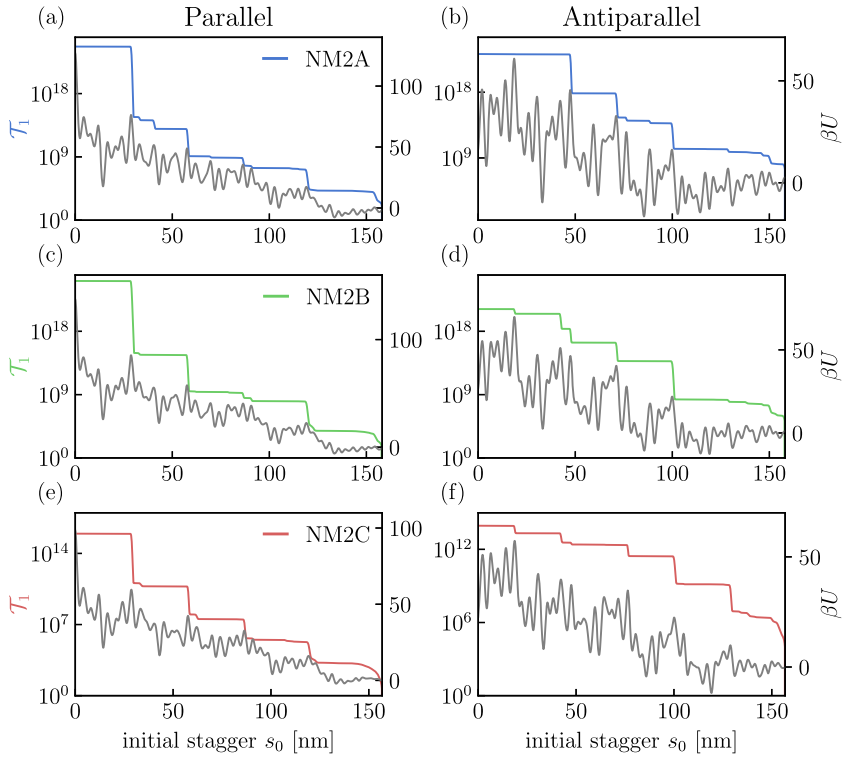

Figure 4. MFPT $\mathcal{T}_1$ calculated numerically from equation (10) as a function of the initial stagger position s_0 in either parallel (left) or antiparallel (right) configurations. Shown are the variants NM2A (blue, (a) and (b)), NM2B (green, (c) and (d)) and NM2C (red, (e) and (f)). In all cases the MFPT decreases monotonically with increasing s_0, however, $\mathcal{T}_1$ shows significant decreases at only a few specific positions that coincide with certain potential barriers of the underlying energy landscapes. While $\mathcal{T}_1$ for NM2A and NM2B are very similar, the one for NM2C is much smaller.

not in quantitative absolute values. This makes the exact values for the MFPTs arbitrary. We however keep length dimensions in units of nm to better compare distances with the underlying biophysical system.

In figure 4 we show calculated MFPTs as a function of the initial stagger s_0 for different NM2-variants in a semi-log plot for parallel and antiparallel configurations. As expected, $\mathcal{T}_1$ decreases monotonically for increasing initial staggers s_0 as the overall distance to reach the absorbing target becomes smaller. Surprisingly, however, this decrease occurs in only a few discrete drops, which seem to correspond to specific barriers in the complex energy landscape. Moreover these drops can be very large, with downward jumps of several orders of magnitude. Together, these results imply that the MFPTs are both robust and very sensitive to initial stagger values, depending whether one starts in one of the plateau regions or close to an edge. Regarding the different isoforms, we see from figure 4 that NM2A and NM2B behave very similarly, while NM2C is much less stable, with the MFPTs being smaller by four or even six orders of magnitude for parallel and antiparallel rods, respectively. This agrees with the fact that NM2C forms smaller minifilaments with approximately only 14 motor proteins compared to otherwise 30 [84, 86]. We also note that the difference between NM2A and NM2B seem to be a bit larger for the antiparallel configurations. Interestingly, for parallel rod configuration, the four most noticeably drops of the MFPT are approximately spaced with a 196 residue repeat ($\sim$28.54 nm), which is well known for the charge repeat of NM2 molecules [97, 99, 100].

It is clear that starting after a prominent barrier will result in a lower MFTP. However, the double-integral formula of the MFPT in equation (10) not only takes local information (s_0) into account, but also encodes global information of the energy landscape, because many different paths can be taken towards the endpoint. This makes it notoriously difficult to answer the question which energy barriers are central to the shape of the MFPT in complex landscapes as in the case of our NM2-example. Here we see that overcoming certain potential barriers substantially decreases the MFPT $\mathcal{T}_1$, while others (possible even of same height) seemingly leave the MFPT unchanged. In order to better understand this important point, we next turn to a coarse-graining procedure that asks the question which features have to be kept when going to larger scales.

In figure 5 we additionally report our results for all possible combinations of the three different isoforms. While the ordering does not matter here (different from our earlier treatment that included bending [97]), the alignment is very important. We see that the antiparallel configurations (green) typically

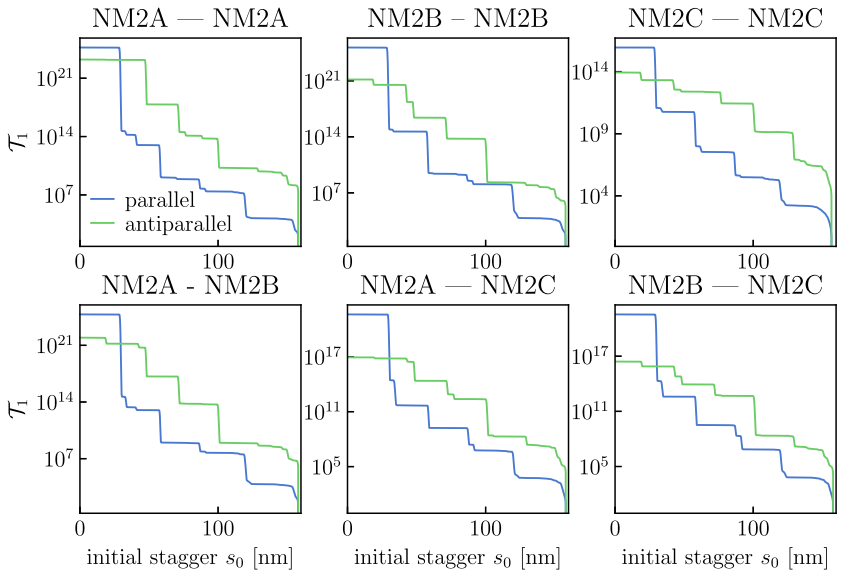

Figure 5. Direct comparison between the MFPT $\mathcal{T}_1$ for parallel (blue) and antiparallel (green) NM2-dimer configurations for all different variant combinations. For the majority of initial staggers the antiparallel rod configuration has larger $\mathcal{T}_1$ compared to parallel alignment, suggesting that antiparallel NM2-dimers are more stable. Only at small s_0 parallel NM2-rods have higher $\mathcal{T}_1$. All combinations involving NM2C have much smaller values for $\mathcal{T}_1$.

have higher values for the MFPT $\mathcal{T}_1$ than the parallel ones (blue), indicating the importance of the bipolar architecture. Only for very small staggers does the parallel configuration become more stable. Moreover we see again that combinations involving NM2C are always much less stable than the ones involving only NM2A and NM2B.

4. Coarse-graining to master equation

4.1. One-step master equation

Our numerical treatment of equation (10), which is based on continuous-state dynamics of an overdamped Fokker–Planck equation, has shown a pattern in the MFPT as a function of stagger that requires an explanation in terms of the key features of the underlying complex energy landscape. To identify these features, we now coarse-grain the continuous-state dynamics into a set of discrete states to further analyze the MFPT as a function of the initial stagger and learn more about the connection between energy landscape and the shape of the MFPT. The motivation hereby is twofold. First, the existence of high energy barriers that are significant to the thermal energy k_BT (see figure 3) allows us to motivate a clear time-scale separation such that a diffusing particle would spend the majority of its time located in valleys of the energy landscape before eventually escaping the barrier—a situation well described by stochastic transitions on a discrete network in terms of a Markovian jump process. Second, the MFPT until a NM2-dimer detaches has, compared to the underlying energy landscape, a relatively simple shape suggesting that only a selected few potential barriers and minima contribute to the overall average time needed. As seen in figure 4 the shape of the MFPT is characterized by a of number pronounced decreases which coincide with the position of specific potential barriers. Unfortunately this feature remains elusive for the continuous-state description as the expression used to calculate the MFTP $\mathcal{T}_1$ in equation (10) poses a non-trivial transformation of the underlying energy landscape.

Within the coarse-graining procedure we treat each local minima of the corresponding NM2 energy landscapes as a discrete state in the network description. Being in a state is therefore equivalent to residing in the associated local basin. By splitting the energy landscape into a number of N basins (compare figure 6(b)), delimited by their adjacent potential maxima, the resulting Markovian network is then described by the set $\Omega = \{0, 1, \ldots, N-1\}$ of N discrete states. Local minima in the energy landscape are identified numerically using the `signal.argrelmin` function of the Python library `SciPy` [116]. The network dynamics follow the master equation

$$\partial_t p_i(t) = \sum_{j=1}^{N-1} [w_{ji} p_j(t) - w_{ij} p_i(t)]. \tag{11}$$

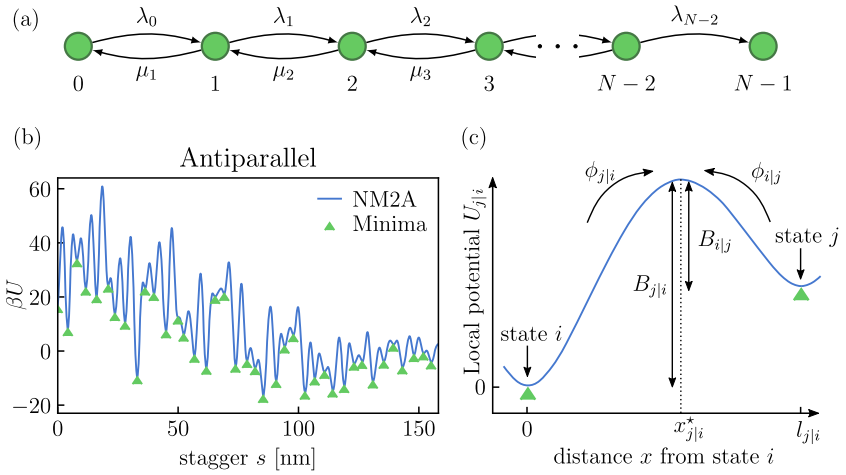

Figure 6. Master equation. (a) Network of the coarse-grained Markov jump process describing the minima-to-minima dynamics of the original continuous-state dynamics. States correspond to the identified minimas and transitions rate λ_i and μ_i are obtained as detailed in the main text. The last state $N-1$ describes the detachment of a NM2-dimer, i.e., it is absorbing. (b) Energy landscape of the antiparallel NM2A dimer without pulling force (i.e. $F = 0$ pN). Highlighted are all 39 local potential minima (green) each corresponding to a discrete state in the network description of the coarse-grained system. (c) Local energy landscape $U_{j|i}$ between adjacent states i and j which are separated by a barrier located at position $x^\star_{j|i}$. If both barriers are high (e.g. $B_{j|i}$ and $B_{i|j} > k_\mathrm{B}T$), the systems locally equilibrates prior to the next transition and can be described using a Markov jump process. The splitting probability $\phi_{j|i}$ denotes the probability that the next transition $i \to j$ takes place.

Here $p_i(t)$ represents the occupation probability to be in state i at time t and w_{ij} denotes the transition rate to pass from state i to state j. Transitions only occur between directly neighboring states due to the considered problem of stagging two neighboring rods. Therefore, the master equation (11) may be re-written in a one-step form as

$$\partial_t p_i(t) = \lambda_{i-1} p_{i-1}(t) + \mu_{i+1} p_{i+1}(t) - (\lambda_i + \mu_i) p_i(t), \tag{12}$$

where we define the transition rates $\lambda_i = w_{i,i+1}$ and $\mu_i = w_{i,i-1}$ (transition rates between non-neighboring states vanish). Figure 6(a) shows the corresponding reaction network. The MFPT is now identified with the time at which the transition $N-2 \to N-1$ into the absorbing state takes place. As before, the state $N = 0$ is reflecting.

4.2. Transition rates

Without loss of generality, we now choose the NM2A dimer in antiparallel configuration as an exemplary case. Figure 6(b) shows the $N = 39$ states that we obtain numerically from the corresponding energy landscape. For Markovian network dynamics, the exit rate r_i (or inverse lifetime) of the state i, i.e., the time that passes until the state changes, is exponentially distributed according to $p_i^{\mathrm{exit}}(t) = r_i \exp(-r_i t)$ with $r_i = 1/\langle t \rangle_i^{\mathrm{exit}} = \sum_{j \in \mathcal{N}_i} w_{ij}$ (here $\mathcal{N}_i$ labels the neighbors of state i). The exit time distribution is independent of the final state j, allowing us to write the (splitting) probability of the transition from state i to j (i.e., that the next visited state will be j conditioned on that the system is in state i) as $\phi_{j|i} = w_{ij}/r_i$. Under these considerations the transition rates are then obtained as

$$w_{ij} = \frac{\phi_{j|i}}{\langle t \rangle_i^{\mathrm{exit}}}. \tag{13}$$

Quantities like the average exit time and the splitting probability entering equation (13) can be related to a *conditional* FPT problem [78, 117]. Here, one seeks the first time a system reaches a specific target state conditioned on that it has not yet reached any other (of possibly arbitrary many) target states before. Based on this framework and using the renewal theorem [118], results for the splitting probability and the mean exit time have been derived recently for general networks with a 'star-like' topology [117]. The 'inner' node is thereby the starting state and all 'outer' nodes are target states. A line network as we consider it here is a particular simple case of this network topology. Hereby, assuming that the full network dynamics between two network states evolve according to a continuous space-time overdamped Markovian diffusion, the *splitting probability* $\phi_{j|i}$ that starting from some state i the neighboring state visited next will be state j is given by the explicit expression

$$\phi_{j|i} = \frac{1/I^{(1)}_{j|i}}{\sum_{k \in \mathcal{N}_i} 1/I^{(1)}_{k|i}} \tag{14}$$

and is normalized such that $\sum_{j\in\mathcal{N}_i}\phi_{j|i}=1$. The second important quantity required to obtain transition rates is the mean exit time of state i which is obtained using the same framework via the expression

$$\langle t\rangle_i^{\text{exit}}=\sum_k \phi_{k|i}I_{k|i}^{(2)}, \tag{15}$$

where the two auxiliary integrals $I_{j|i}^{(1)}$ and $I_{j|i}^{(2)}$ in equations (14) and (15) are defined [117] as

$$I_{j|i}^{(1)}=\int_0^{l_{j|i}}\mathrm{d}y_1\;\; g_{j|i}^{(1)}\quad\text{with}\quad g_{j|i}^{(1)}=\frac{1}{D_{j|i}}\,\mathrm{e}^{\beta U_{j|i}(y_1)}, \tag{16}$$

$$I_{j|i}^{(2)}=\int_0^{l_{j|i}}\mathrm{d}y_1\int_0^{y_2}\mathrm{d}y_2\;\; g_{j|i}^{(2)}\quad\text{with}\quad g_{j|i}^{(2)}=\frac{1}{D_{j|i}}\,\mathrm{e}^{\beta U_{j|i}(y_1)-\beta U_{j|i}(y_2)}. \tag{17}$$

Here $l_{j|i}$ denotes the distance between two adjacent minima (i.e. states i and j) defined through the underlying energy landscape and $U_{j|i}$ is the *local* energy landscape relative to the value at state i between states i and j as schematically depicted in figure 6. For the purpose of calculating the transitions rate between two neighboring states we therefore identify their intervening local potentials and numerically compute the integrals in equations (16) and (17) employing the trapezoid rule function `integrate.trapezoid` as implemented in the python library `SciPy` [116].

4.3. Mean first-passage time

After identifying all network states and calculating the corresponding transition rates w_{ij}, and thus λ_i and μ_i of equation (12), the Markov jump process is now fully specified. Therefore, we are able to determine the MFPT, i.e. the average detachment time of NM2-dimers, within the coarse-grained network description of the minima-to-minima dynamics of a diffusing Brownian particle in the original overdamped Fokker–Planck picture. As for the continuous system, the corresponding absorbing state is hereby always placed in the last state such that reaching it corresponds to the detachment of the NM2-molecules.

In analogy to the analytical solution of the MFPT in equation (10), which holds for a Fokker–Planck equation for overdamped Langevin dynamics in an external potential U, for a Markov process confined between mixed boundaries (a reflecting and b absorbing with $a<b$) the MFPT is given by [78, 119]

$$\mathcal{T}_1(i_0;a,b)=\sum_{i=i_0}^{b-1}\sum_{n=a}^{i}\lambda_n^{-1}\Pi_{n+1,i}\quad\text{with}\quad\Pi_{i,j}=\frac{\mu_i\mu_{i+1}\dots\mu_j}{\lambda_i\lambda_{i+1}\dots\lambda_j}\quad\text{for } i\leqslant j, \tag{18}$$

where i_0 is the starting state, a the reflecting state, and b the absorbing target state. In our case this MFPT has to be calculated as a function of the initial stagger i_0 and a and b are set to the first and last state, respectively. This calculation now is much more computationally efficient than the continuum version. Figures 7(a) and (b) show a direct comparison between the MFPT $\mathcal{T}_1$ computed using equation (10) (lines) and equation (18) (symbols) for the NM2A-dimer. Clearly, the results of the two different approaches agree very well with each other, thus validating our coarse-graining approach. The same picture emerges for the other NM2 variants. We additionally plot the mean exit-time $\langle t\rangle_i^{\text{exit}}$ from equation (15) as bars. Interestingly, the experimentally observed staggers (black arrows) for the parallel configuration corresponds to large values for $\langle t\rangle_i^{\text{exit}}$. In particular, the most prominent stagger at $s=14.3$ nm corresponds to the highest overall mean exit-time. While the mean exit-times corresponding to experimentally observed staggers for antiparallel alignment are not notably large on a global scale, they are indeed large compared to adjacent states. This suggests that these staggers confer some local robustness against perturbations. We additionally note that the periodicity between small mean exit-times seems to follow the characteristic 98-residue repeat pattern already encountered earlier.

4.4. Predicting jumps

The relatively simple shape of the MFPT and the characteristic feature to decrease substantially over several orders of magnitude by only a slight variation of the initial stagger position between two NM2-molecules in the detachment process remained elusive in the continuous description. The discrete nature of the Markov jump process now allows us to gain further insights in the behavior of the MFPT of the detachment process of two aligned NM2-molecules. We first note that an exploration of the complete network topology (i.e. the complete energy landscape) takes place if the system is initially prepared in state $i_0=0$. Then is has to visit each state at least once before reaching the absorbing target at the other end of the network chain. For this

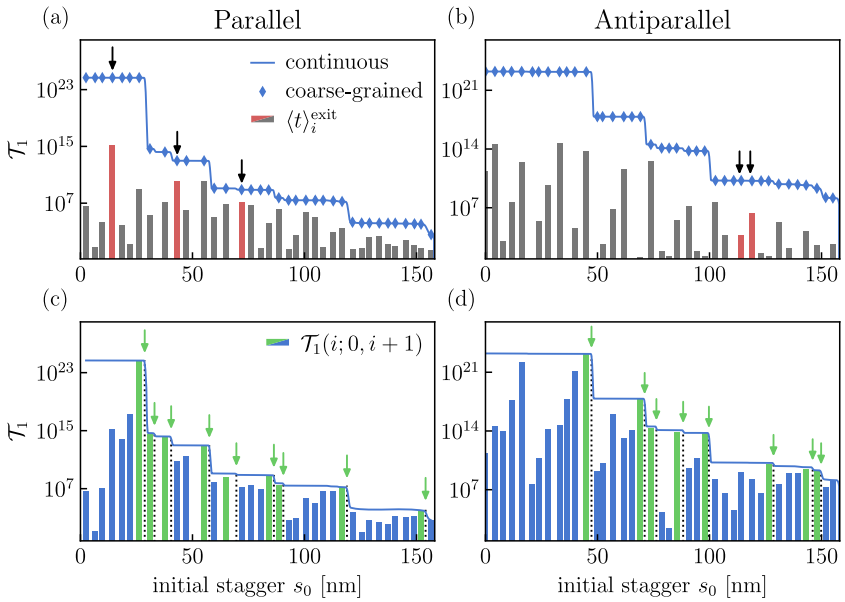

Figure 7. MFPTs $\mathcal{T}_1$ for the original continuum system compared to its coarse-grained counterpart. (a) and (b) Comparison between the MFPT $\mathcal{T}_1$ of the continuous description equation (10) and the coarse-grained network equation (18) for (a) parallel and (b) antiparallel NM2A-dimer configurations. Mean exit-times $\langle t \rangle_i^{\text{exit}}$ (equation (15)) are depicted as bars. Experimental staggers (black arrows) are not located at positions of large drops and are characterized by comparatively larger mean exit-times to their neighbors (red bars), ensuring local robustness. (c) and (d) Single MFPTs $\mathcal{T}_1(i;0,i+1)$ from state i to $i+1$ are denoted as bars for the (c) parallel and (d) antiparallel cases. Largest contributions that give rise to jumps in the shape of the overall MFPT are highlighted in green. Predictions of the large jumps obtained using the network description as detailed in the main text are highlighted with green arrows and dotted lines and agree very well with the drops in the full solution.

case equation (18) is explicitly given by

$$\mathcal{T}_1(0;0,b) = \sum_{i=0}^{b-1}\sum_{n=0}^{i} \lambda_n^{-1}\Pi_{n+1,i} = \underbrace{\lambda_0^{-1}}_{i=0} + \underbrace{\lambda_0^{-1}\Pi_{1,1} + \lambda_1^{-1}}_{i=1} + \underbrace{\lambda_0^{-1}\Pi_{1,2} + \lambda_1^{-1}\Pi_{2,2} + \lambda_2^{-1}}_{i=2}$$
$$+ \cdots + \underbrace{\lambda_0^{-1}\Pi_{1,b-1} + \lambda_1^{-1}\Pi_{2,b-1} + \cdots + \lambda_{b-2}^{-1}\Pi_{b-1,b-1} + \lambda_{b-1}^{-1}}_{i=b-1}. \tag{19}$$

For a process that starts at a transient initial state m with $0 < m < b$, i.e. away from the reflecting state, the lower bound of the first sum in equation (19) has to be changed from $i = 0$ to $i = m$. Explicitly writing out the double sum in this way shows that terms of the outer sum (summation over i) correspond to *single* MFPTs $\mathcal{T}_1(i;0,i+1)$ from state i to $i+1$ while keeping the reflective state unaltered in state 0. That is, irrespective of where the systems starts, it is always allowed to visit state '0' again. For illustration, consider the single MFPT $\mathcal{T}_1(2;0,3)$ for the transition $2 \to 3$, i.e. the case $i = 2$ above. The last contribution, λ_2^{-1}, is the time needed for the direct path from state 2 to 3. Depending on the transitions rates (e.g. when $\mu_2 > \lambda_2$) the system might however also transition backwards to state 1 or even 0 before finally reaching the absorbing target in state 3 for the first time. These additional paths are accounted for by the corresponding inverse rates and the weighting factor $\Pi_{2,2}$ as defined in equation (18). Consequently, we may express the MFPT as a sum over all individual single MFPTs as

$$\mathcal{T}_1(0;0,b) = \sum_{i=0}^{b-1} \mathcal{T}_1(i;0,i+1) = \mathcal{T}_1(0;0,1) + \mathcal{T}_1(1;0,2) + \cdots + \mathcal{T}_1(b-1;0,b), \tag{20}$$

where the systems starts initially in state 0. In the same way as before, if one starts in a state $0 < m < b$ the summation starts from $i = m$.

A decomposition into single MFPTs now makes it possible to distinguish between larger and smaller contributions to the full MFPT. Single MFPTs from state i to state $i+1$ (leaving the reflecting state 0 unchanged) are shown in figures 7(c) and (d) for the network description of the NM2-dimer system for antiparallel and parallel configuration, respectively. It becomes immediately evident that the single MFPTs are highly irregular and vary over several orders of magnitude depending on the initial state i_0. Based on this coarse-grained description we are now able to identify the largest contributions towards the average detachment time of the NM2 dimer (marked in green). This implies that if we were to initially prepare the

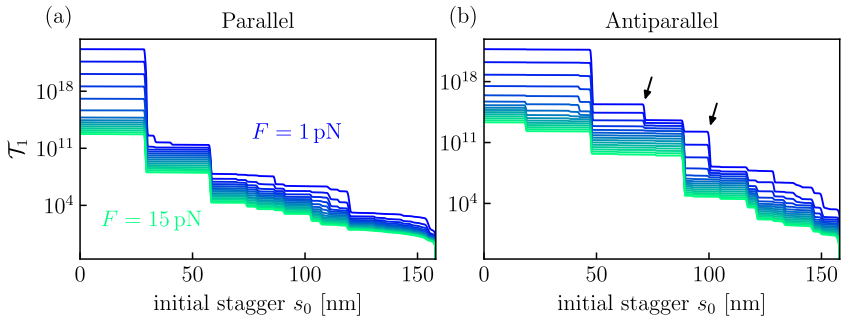

Figure 8. MFPT $\mathcal{T}_1$ as a function of the initial staggering s_0 between two aligned NM2-molecules for variable pulling forces F ranging from $F = 1$ pN (blue) to $F = 15$ pN (teal) in steps of one. Depicted are the MFPTs for the NM2A variant in (a) parallel and (b) antiparallel configurations. While the shape for parallel configuration does not change much, the antiparallel dimer shows qualitative changes as sudden changes in $\mathcal{T}_1$ vanish by increasing the pulling forces, at positions highlighted by the black arrows.

system in state $m > i^*$, where i^* denotes the state with the largest single MFPT $\mathcal{T}_1(i; 0, i+1)$, we would expect a substantial decrease in the time needed until the NM2-dimer detaches as all contributions (and therefore the largest too) of single MFPTs for states $< m$ drop out, i.e., the sum in equation (20) starts at $i = m$. Analogously, the next and all further drops in the MFPT can be identified using the same principle, namely finding the next largest single MFPT and choosing the initial state accordingly. In figures 7(c) and (d) we show that indeed our procedure of identifying the relevant minima and barriers (green bars) predicts the observed drops in the full solutions (green arrows and dotted lines), both for parallel (c) and antiparallel (d) configurations. Thus our main question has now been answered, namely which energy barriers lead to the large drops in the MFPTs.

5. Mean first-passage time under mechanical load

Finally we address the question how the MFPT changes if we 'tilt' the energy landscape by an additional pulling force as motivated in section 2.2. More precisely, in our biophysical example of the NM2 assembly landscape, we now study how the average time until NM2-dimer detachment behaves under a variable mechanical load that is applied along the dimer main axis.

To compute the MFPT for the driven system we insert the tilted energy landscape equation (4) into equation (10). Resulting MFPTs of antiparallel and parallel alignments are depicted in figure 8 for different pulling forces F. As one would expect, the application of the pulling force results in faster MFPTs to reach the absorbing border, i.e., faster detachment of aligned NM2-molecules. Interestingly, the MFPT for the parallel NM2-dimer mostly keeps its qualitative shape unchanged. This means that the set of important potential barrier that lead to large decreases in the MPFT remains the same even under the presence of external pulling. In contrast, shapes of the MFPT for antiparallel orientation undergo more pronounced changes under the influence of external pulling forces. On one hand, overcoming previously identified significant potential barriers at e.g. $\approx$ 72 nm or $\approx$98 nm (black arrows) now does not result in a large decrease of the MFPT anymore. On the other hand, overcoming new potential barriers at e.g. $\approx$87 nm or $\approx$117 nm now results in a large decrease of the MFPT. We suggest that this apparent difference between antiparallel and parallel alignment might have biophysical consequences during NM2 minifilament assembly and filament splitting during partition events under mechanical load.

6. Conclusions

Here we have studied the MFPT for rough, complex one-dimensional energy landscapes. As a biophysical relevant example we considered the self-assembly process of the three different isoforms A, B and C of NM2. We theoretically studied the average time until two aligned NM2-molecules (i.e. the nucleation point for minifilament assembly) detach with and without an additional pulling force as a FPT problem on complex energy landscapes derived from the amino acid sequences of different NM2-variants. We demonstrated how the MFPT of highly complex and rugged one-dimensional landscapes can be obtained by coarse-graining the underlying continuous dynamics described by the Fokker–Planck equation into a discrete-state continuous-time Markov jump process, that is a master equation. Our numerical procedure not only gives perfect agreement between the two descriptions, it also allowed us to decompose the MFPT into its different contributions and from there to identify the relevant barriers that lead to the sudden drops

in lifetime. Overall, our work shows how one can better understand the relevant features of a complex energy landscape by systematically studying the corresponding MFPTs.

Because here we restrict ourselves to the one-dimensional case of straight rods, our MFPT-treatment does not predict the experimentally observed staggers as well as did our earlier treatment that included the bending energy of the rods splaying away from the main axis due to electrostatic repulsion [97]. Nevertheless our specific results for NM2 also seem to be very important to better understand the biophysics of NM2-minifilaments and in particular shed new light on the role of physical force for their assembly and stability. In detail, we found that the experimentally known staggers are in regions of high stability (away from the jumps), that they exhibit large local exit times, that dimers involving NM2C are much less stable (shorter lifetimes) than the ones involving NM2A and NM2B, that the difference between NM2A and NM2B is larger for the antiparallel configurations, that antiparallel configurations are more stable without force, but also show larger changes under pulling force. In the future, it would be very interesting to extend this approach to the energy landscapes including bending as well as to go beyond dimers and to also consider high-order assemblies. This, however, would require to treat high-dimensional energy landscapes which constitutes formidable numerical and mathematical challenges.

Acknowledgments

We acknowledge funding through the Max Planck School Matter to Life, supported by the German Federal Ministry of Education and Research (BMBF) in collaboration with the Max Planck Society. USS is supported by the Deutsche Forschungsgemeinschaft (DFG, German Research Foundation) under the Excellence Strategy through EXC 2181/1-390900948 (the Heidelberg STRUCTURES Excellence Cluster) and EXC 2082/1-390761711 (the Heidelberg-Karlsruhe Cluster of Excellence 3DMM2O). He also is a member of the Interdisciplinary Center for Scientific Computing (IWR). We thank Tom Kaufmann, Justin Grewe, Kai Weißenbruch, Martin Bastmeyer and Jordan Beach for stimulating discussions.

Data availability statement

The data that support the findings of this study are openly available at the following URL/DOI: https://doi.org/10.5281/zenodo.6612354.

ORCID iDs

Rick Bebon https://orcid.org/0000-0003-2187-0008
Ulrich S Schwarz https://orcid.org/0000-0003-1483-640X

References

[1] Wales D J 2003 *Energy Landscapes: Applications to Clusters, Biomolecules and Glasses* (Cambridge: Cambridge University Press)
[2] Espenson J H 1995 *Chemical Kinetics and Reaction Mechanisms* (New York: McGraw-Hill)
[3] Houston P L 2012 *Chemical Kinetics and Reaction Dynamics* (Mineola, New York: Dover Publications)
[4] Heuer A 2008 Exploring the potential energy landscape of glass-forming systems: from inherent structures via metabasins to macroscopic transport *J. Phys.: Condens. Matter* **20** 373101
[5] Garrahan J P and Chandler D 2002 Geometrical explanation and scaling of dynamical heterogeneities in glass forming systems *Phys. Rev. Lett.* **89** 035704
[6] Tănase-Nicola S and Kurchan J 2003 Topological methods for searching barriers and reaction paths *Phys. Rev. Lett.* **91** 188302
[7] Nussinov R and Wolynes P G 2014 A second molecular biology revolution? the energy landscapes of biomolecular function *Phys. Chem. Chem. Phys.* **16** 6321–2
[8] Wales D J 2018 Exploring energy landscapes *Annu. Rev. Phys. Chem.* **69** 401–25
[9] Neupane K, Manuel A P and Woodside M T 2016 Protein folding trajectories can be described quantitatively by one-dimensional diffusion over measured energy landscapes *Nat. Phys.* **12** 700–3
[10] Satija R, Berezhkovskii A M and Makarov D E 2020 Broad distributions of transition-path times are fingerprints of multidimensionality of the underlying free energy landscapes *Proc. Natl Acad. Sci. USA* **117** 27116–23
[11] Zhang B and Wolynes P G 2017 Genomic energy landscapes *Biophys. J.* **112** 427–33
[12] Chou T 1999 Kinetics and thermodynamics across single-file pores: solute permeability and rectified osmosis *J. Chem. Phys.* **110** 606–15
[13] Bauer W R and Nadler W 2010 Thermodynamics of competitive molecular channel transport: application to artificial nuclear pores *PLoS One* **5** e15160
[14] Berezhkovskii A M, Pustovoit M A and Bezrukov S M 2002 Channel-facilitated membrane transport: transit probability and interaction with the channel *J. Chem. Phys.* **116** 9952–6
[15] Zilman A 2009 Effects of multiple occupancy and interparticle interactions on selective transport through narrow channels: theory versus experiment *Biophys. J.* **96** 1235–48

[16] Jülicher F, Ajdari A and Prost J 1997 Modeling molecular motors *Rev. Mod. Phys.* **69** 1269
[17] Kolomeisky A B 2013 Motor proteins and molecular motors: how to operate machines at the nanoscale *J. Phys.: Condens. Matter* **25** 463101
[18] Maisuradze G G, Liwo A and Scheraga H A 2010 Relation between free energy landscapes of proteins and dynamics *J. Chem. Theory Comput.* **6** 583–95
[19] Mukherjee S and Warshel A 2012 Realistic simulations of the coupling between the protomotive force and the mechanical rotation of the F_0-ATPase *Proc. Natl. Acad. Sci. USA* **109** 14876–81
[20] Mukherjee S, Alhadeff R and Warshel A 2017 Simulating the dynamics of the mechanochemical cycle of myosin-V *Proc. Natl. Acad. Sci. USA* **114** 2259–64
[21] Hummer G and Szabo A 2001 Free energy reconstruction from nonequilibrium single-molecule pulling experiments *Proc. Natl. Acad. Sci. USA* **98** 3658–61
[22] Harris N C, Song Y and Kiang C-H 2007 Experimental free energy surface reconstruction from single-molecule force spectroscopy using Jarzynski's equality *Phys. Rev. Lett.* **99** 068101
[23] Gupta A N, Vincent A, Neupane K, Yu H, Wang F and Woodside M T 2011 Experimental validation of free-energy-landscape reconstruction from non-equilibrium single-molecule force spectroscopy measurements *Nat. Phys.* **7** 631–4
[24] van Kampen N G 1992 *Stochastic Processes in Physics and Chemistry* (Amsterdam: Elsevier)
[25] Redner S 2001 *A Guide to First-Passage Processes* (Cambridge: Cambridge University Press)
[26] Metzler R, Redner S and Oshanin G 2014 *First-Passage Phenomena and Their Applications* (Singapore: World Scientific)
[27] Kramers H A 1940 Brownian motion in a field of force and the diffusion model of chemical reactions *Physica* **7** 284–304
[28] Schulten K, Schulten Z and Szabo A 1981 Dynamics of reactions involving diffusive barrier crossing *J. Chem. Phys.* **74** 4426–32
[29] Hänggi P, Talkner P and Borkovec M 1990 Reaction-rate theory: fifty years after Kramers *Rev. Mod. Phys.* **62** 251
[30] Szabo A, Schulten K and Schulten Z 1980 First passage time approach to diffusion controlled reactions *J. Chem. Phys.* **72** 4350–7
[31] Bénichou O, Chevalier C, Klafter J, Meyer B and Voituriez R 2010 Geometry-controlled kinetics *Nat. Chem.* **2** 472–7
[32] Rotbart T, Reuveni S and Urbakh M 2015 Michaelis–Menten reaction scheme as a unified approach towards the optimal restart problem *Phys. Rev.* E **92** 060101
[33] Singh D and Chaudhury S 2017 Statistical properties of fluctuating enzymes with dynamic cooperativity using a first passage time distribution formalism *J. Chem. Phys.* **146** 145103
[34] Robin T, Reuveni S and Urbakh M 2018 Single-molecule theory of enzymatic inhibition *Nat. Commun.* **9** 779
[35] Condamin S, Bénichou O, Tejedor V, Voituriez R and Klafter J 2007 First-passage times in complex scale-invariant media *Nature* **450** 77–80
[36] Eliazar I, Koren T and Klafter J 2007 Searching circular DNA strands *J. Phys.: Condens. Matter* **19** 065140
[37] Bénichou O, Loverdo C, Moreau M and Voituriez R 2011 Intermittent search strategies *Rev. Mod. Phys.* **83** 81
[38] Chou T and D'Orsogna M R 2014 First passage problems in biology *First-passage Phenomena and Their Applications* (Singapore: World Scientific) pp 306–45
[39] Iyer-Biswas S and Zilman A 2016 First-passage processes in cellular biology *Adv. Chem. Phys.* **160** 261–306
[40] Bénichou O and Voituriez R 2014 From first-passage times of random walks in confinement to geometry-controlled kinetics *Phys. Rep.* **539** 225–84
[41] Godec A and Metzler R 2016 First passage time distribution in heterogeneity controlled kinetics: going beyond the mean first passage time *Sci. Rep.* **6** 20349
[42] Godec A and Metzler R 2016 Universal proximity effect in target search kinetics in the few-encounter limit *Phys. Rev.* X **6** 041037
[43] Grebenkov D S, Metzler R and Oshanin G 2018 Towards a full quantitative description of single-molecule reaction kinetics in biological cells *Phys. Chem. Chem. Phys.* **20** 16393–401
[44] Grebenkov D S 2016 Universal formula for the mean first passage time in planar domains *Phys. Rev. Lett.* **117** 260201
[45] Erdmann T and Schwarz U S 2004 Stochastic dynamics of adhesion clusters under shared constant force and with rebinding *J. Chem. Phys.* **121** 8997–9017
[46] Erdmann T and Schwarz U S 2007 Impact of receptor-ligand distance on adhesion cluster stability *Eur. Phys. J.* E **22** 123–37
[47] Blom K and Godec A 2021 Criticality in cell adhesion *Phys. Rev.* X **11** 031067
[48] Schwarz U S, Erdmann T and Bischofs I B 2006 Focal adhesions as mechanosensors: the two-spring model *Biosystems* **83** 225–32
[49] Erdmann T and Schwarz U S 2004 Stability of adhesion clusters under constant force *Phys. Rev. Lett.* **92** 108102
[50] Erdmann T, Albert P J and Schwarz U S 2013 Stochastic dynamics of small ensembles of non-processive molecular motors: the parallel cluster model *J. Chem. Phys.* **139** 175104
[51] Erdmann T and Schwarz U S 2012 Stochastic force generation by small ensembles of myosin II motors *Phys. Rev. Lett.* **108** 188101
[52] E Baschek J, Klein H C R and Schwarz U S 2012 Stochastic dynamics of virus capsid formation: direct versus hierarchical self-assembly *BMC Biophys.* **5** 22
[53] Chekmarev S F 2021 First-passage times in protein folding: exploring the native-like states vs overcoming the free energy barrier *Phys. Chem. Chem. Phys.* **23** 17856–65
[54] Micheelsen M A, Rischel C, Ferkinghoff-Borg J, Guerois R and Serrano L 2003 Mean first-passage time analysis reveals rate-limiting steps, parallel pathways and dead ends in a simple model of protein folding *Europhys. Lett.* **61** 561
[55] Shillcock J and Seifert U 1998 Escape from a metastable well under a time-ramped force *Phys. Rev.* E **57** 7301
[56] Hummer G and Szabo A 2003 Kinetics from nonequilibrium single-molecule pulling experiments *Biophys. J.* **85** 5–15
[57] Dudko O, Hummer G and Szabo A 2006 Intrinsic rates and activation free energies from single-molecule pulling experiments *Phys. Rev. Lett.* **96** 108101
[58] Dudko O K, Mathé J, Szabo A, Meller A and Hummer G 2007 Extracting kinetics from single-molecule force spectroscopy: nanopore unzipping of DNA hairpins *Biophys. J.* **92** 4188–95
[59] Dudko O K, Hummer G and Szabo A 2008 Theory, analysis, and interpretation of single-molecule force spectroscopy experiments *Proc. Natl. Acad. Sci. USA* **105** 15755–60
[60] Hu Z, Cheng L and Berne B J 2010 First passage time distribution in stochastic processes with moving and static absorbing boundaries with application to biological rupture experiments *J. Chem. Phys.* **133** 034105
[61] Abkenar M, Gray T H and Zaccone A 2017 Dissociation rates from single-molecule pulling experiments under large thermal fluctuations or large applied force *Phys. Rev.* E **95** 042413
[62] Viswanathan G M, Afanasyev V, Buldyrev S V, Murphy E J, Prince P A and Stanley H E 1996 Lévy flight search patterns of wandering albatrosses *Nature* **381** 413–5

[63] Viswanathan G M, Da Luz M G E, Raposo E P and Stanley H E 2011 *The Physics of Foraging: An Introduction to Random Searches and Biological Encounters* (Cambridge: Cambridge University Press)
[64] Bell W J 2012 *Searching Behaviour: The Behavioural Ecology of Finding Resources* (Belin: Springer)
[65] Palyulin V V, Chechkin A V and Metzler R 2014 Lévy flights do not always optimize random blind search for sparse targets *Proc. Natl. Acad. Sci. USA* **111** 2931–6
[66] Howard C B 2018 *Random Walks in Biology* (Princeton, NJ: Princeton University Press)
[67] Johnson A R, Wiens J A, Milne B T and Crist T O 1992 Animal movements and population dynamics in heterogeneous landscapes *Landscape Ecol.* **7** 63–75
[68] Lloyd A L and May R M 2001 How viruses spread among computers and people *Science* **292** 1316–7
[69] Volovik D and Redner S 2010 First-passage properties of bursty random walks *J. Stat. Mech.* P06018
[70] Hufnagel L, Brockmann D and Geisel T 2004 Forecast and control of epidemics in a globalized world *Proc. Natl. Acad. Sci. USA* **101** 15124–9
[71] Ben-Avraham D and Havlin S 2000 *Diffusion and Reactions in Fractals and Disordered Systems* (Cambridge: Cambridge University Press)
[72] Mantegna R N and Stanley H E 1999 *Introduction to Econophysics: Correlations and Complexity in Finance* (Cambridge: Cambridge University Press)
[73] Schuss Z, Singer A and Holcman D 2007 The narrow escape problem for diffusion in cellular microdomains *Proc. Natl. Acad. Sci. USA* **104** 16098–103
[74] Zwanzig R 1988 Diffusion in a rough potential *Proc. Natl Acad. Sci. USA* **85** 2029–30
[75] Palyulin V V and Metzler R 2012 How a finite potential barrier decreases the mean first-passage time *J. Stat. Mech.* L03001
[76] Chupeau M, Gladrow J, Chepelianskii A, Keyser U F and Trizac E 2020 Optimizing Brownian escape rates by potential shaping *Proc. Natl. Acad. Sci. USA* **117** 1383–8
[77] Wagner C and Kiefhaber T 1999 Intermediates can accelerate protein folding *Proc. Natl. Acad. Sci. USA* **96** 6716–21
[78] Li X and Kolomeisky A B 2013 Mechanisms and topology determination of complex chemical and biological network systems from first-passage theoretical approach *J. Chem. Phys.* **139** 144106
[79] Thorneywork A L, Gladrow J, Qing Y, Rico-Pasto M, Ritort F, Bayley H, Kolomeisky A B and Keyser U F 2020 Direct detection of molecular intermediates from first-passage times *Sci. Adv.* **6** eaaz4642
[80] Hartich D and Godec A 2018 Duality between relaxation and first passage in reversible Markov dynamics: rugged energy landscapes disentangled *New J. Phys.* **20** 112002
[81] Hartich D and Godec A 2019 Interlacing relaxation and first-passage phenomena in reversible discrete and continuous space Markovian dynamics *J. Stat. Mech.* 024002
[82] Hartman M A and Spudich J A 2012 The myosin superfamily at a glance *J. Cell Sci.* **125** 1627–32
[83] Alberts B, Johnson A, Lewis J, Morgan D, Raff M, Roberts K, Walter P, Wilson J and Hunt T 2017 *Molecular Biology of the Cell* (New York: Garland Science)
[84] Craig R and Woodhead J L 2006 Structure and function of myosin filaments *Curr. Opin. Struct. Biol.* **16** 204–12
[85] Vicente-Manzanares M, Ma X, Adelstein R S and Horwitz A R 2009 Non-muscle myosin II takes centre stage in cell adhesion and migration *Nat. Rev. Mol. Cell Biol.* **10** 778–90
[86] Dasbiswas K, Hu S, Schnorrer F, Safran S A and Bershadsky A D 2018 Ordering of myosin II filaments driven by mechanical forces: experiments and theory *Phil. Trans. R. Soc.* B **373** 20170114
[87] Niederman R and Pollard T D 1975 Human platelet myosin: II. *In vitro* assembly and structure of myosin filaments *J. Cell Biol.* **67** 72–92
[88] Billington N, Wang A, Mao J, Adelstein R S and Sellers J R 2013 Characterization of three full-length human nonmuscle myosin II paralogs *J. Biol. Chem.* **288** 33398–410
[89] Burnette D T *et al* 2014 A contractile and counterbalancing adhesion system controls the 3D shape of crawling cells *J. Cell Biol.* **205** 83–96
[90] Beach J R, Shao L, Remmert K, Li D, Betzig E and Hammer J A III 2014 Nonmuscle myosin II isoforms coassemble in living cells *Curr. Biol.* **24** 1160–6
[91] Fenix A M, Taneja N, Buttler C A, Lewis J, Van Engelenburg S B, Ohi R and Burnette D T 2016 Expansion and concatenation of nonmuscle myosin IIA filaments drive cellular contractile system formation during interphase and mitosis *Mol. Biol. Cell* **27** 1465–78
[92] Hu S *et al* 2017 Long-range self-organization of cytoskeletal myosin II filament stacks *Nat. Cell Biol.* **19** 133–41
[93] Jiu Y, Kumari R, Fenix A M, Schaible N, Liu X, Varjosalo M, Krishnan R, Burnette D T and Lappalainen P 2019 Myosin-18B promotes the assembly of myosin II stacks for maturation of contractile actomyosin bundles *Curr. Biol.* **29** 81–92
[94] Beach J R and Hammer J A III 2015 Myosin II isoform co-assembly and differential regulation in mammalian systems *Exp. Cell Res.* **334** 2–9
[95] Weißenbruch K, Grewe J, Hippler M, Fladung M, Tremmel M, Stricker K, Schwarz U S and Bastmeyer M 2021 Distinct roles of nonmuscle myosin II isoforms for establishing tension and elasticity during cell morphodynamics *ELife* **10** e71888
[96] Weißenbruch K, Fladung M, Grewe J, Baulesch L, Schwarz U S and Bastmeyer M 2022 Nonmuscle myosin IIA dynamically guides regulatory light chain phosphorylation and assembly of nonmuscle myosin IIB *Eur. J. Cell Biol.* **101** 151213
[97] Kaufmann T L and Schwarz U S 2020 Electrostatic and bending energies predict staggering and splaying in nonmuscle myosin II minifilaments *PLoS Comput. Biol.* **16** e1007801
[98] Ricketson D, Johnston C A and Prehoda K E 2010 Multiple tail domain interactions stabilize nonmuscle myosin II bipolar filaments *Proc. Natl. Acad. Sci. USA* **107** 20964–9
[99] Straussman R, Squire J M, Ben-Ya'acov A and Ravid S 2005 Skip residues and charge interactions in myosin II coiled-coils: implications for molecular packing *J. Mol. Biol.* **353** 613–28
[100] McLachlan A D and Karn J 1982 Periodic charge distributions in the myosin rod amino acid sequence match cross-bridge spacings in muscle *Nature* **299** 226–31
[101] Rosenberg M, Straussman R, Ben-Ya'acov A, Ronen D and Ravid S 2008 MHC-IIB filament assembly and cellular localization are governed by the rod net charge *PLoS One* **3** e1496
[102] Lupas A 1996 Coiled coils: new structures and new functions *Trends Biochem. Sci.* **21** 375–82
[103] Squire J M 1971 General model for the structure of all myosin-containing filaments *Nature* **233** 457–62
[104] Nakasawa T, Takahashi M, Matsuzawa F, Aikawa S, Togashi Y, Saitoh T, Yamagishi A and Yazawa M 2005 Critical regions for assembly of vertebrate nonmuscle myosin II *Biochemistry* **44** 174–83

[105] Geer L Y, Marchler-Bauer A, Geer R C, Han L, He J, He S, Liu C, Shi W and Bryant S H 2010 The NCBI biosystems database *Nucleic Acids Res.* **38** D492–6
[106] McDonnell A V, Jiang T, Keating A E and Berger B 2006 Paircoil2: improved prediction of coiled coils from sequence *Bioinformatics* **22** 356–8
[107] Berger B, Wilson D B, Wolf E, Tonchev T, Milla M and Kim P S 1995 Predicting coiled coils by use of pairwise residue correlations *Proc. Natl. Acad. Sci. USA* **92** 8259–63
[108] Hvidt S, Nestler F H M, Greaser M L and Ferry J D 1982 Flexibility of myosin rod determined from dilute solution viscoelastic measurements *Biochemistry* **21** 4064–73
[109] Hvidt S, Ferry J D, Roelke D L and Greaser M L 1983 Flexibility of light meromyosin and other coiled-coil α-helical proteins *Macromolecules* **16** 740–5
[110] Israelachvili J N 2011 *Intermolecular and Surface Forces* (New York: Academic)
[111] Poon W C K and Andelman D 2006 *Soft Condensed Matter Physics in Molecular and Cell Biology* (Boca Raton, FL: CRC Press)
[112] Beach J R *et al* 2017 Actin dynamics and competition for myosin monomer govern the sequential amplification of myosin filaments *Nat. Cell Biol.* **19** 85–93
[113] Gardiner C W 1985 *Handbook of Stochastic Methods* vol 3 (Berlin: Springer)
[114] Risken H 1996 Fokker–Planck equation *The Fokker-Planck Equation* (Berlin: Springer) pp 63–95
[115] Pavliotis G A 2014 *Stochastic Processes and Applications: Diffusion Processes, the Fokker–Planck and Langevin Equations* (Berlin: Springer)
[116] Virtanen P *et al* (SciPy 1.0 Contributors) 2020 SciPy 1.0: fundamental algorithms for scientific computing in Python *Nat. Methods* **17** 261–72
[117] Hartich D and Godec A 2021 Emergent memory and kinetic hysteresis in strongly driven networks *Phys. Rev.* X **11** 041047
[118] Siegert A J F 1951 On the first passage time probability problem *Phys. Rev.* **81** 617
[119] Goel N S and Richter-Dyn N 2016 *Stochastic Models in Biology* (Amsterdam: Elsevier)